Data Mine

The Pacific OBS Research into Convecting Asthenosphere (ORCA) Experiment

Zachary C. Eilon*[1], James B. Gaherty[2], Lun Zhang[1], Joshua Russell[3], Sean McPeak[4], Joseph Phillips[2], Donald W. Forsyth[3], and Göran Ekström[5]

Abstract

The Pacific ocean-bottom seismometer (OBS) Research into Convecting Asthenosphere (ORCA) experiment deployed two 30-station seismic arrays between 2018 and 2020—a US contribution to the international PacificArray project. The "Young ORCA" array deployed on ~40 Ma central Pacific seafloor had a ~68% data recovery rate, whereas the "Old ORCA" array deployed on ~120 Ma southwest Pacific seafloor had a ~80% recovery rate. We detail here the seismic data quality, spectral characteristics, and engineering challenges of this experiment. We provide information to assist users of this dataset, including OBS orientations and tables of daily data quality for all channels. Preliminary analysis illustrates the utility of these data for surface- and body-wave seismic imaging.

Cite this article as Eilon, Z. C., J. B. Gaherty, L. Zhang, J. Russell, S. McPeak, J. Phillips, D. W. Forsyth, and G. Ekström (2021). The Pacific OBS Research into Convecting Asthenosphere (ORCA) Experiment, *Seismol. Res. Lett.* **93**, 477–493, doi: 10.1785/0220210173.

Supplemental Material

Introduction and Motivation

The Pacific ocean-bottom seismometer (OBS) Research into Convecting Asthenosphere (ORCA) project is a dual array broadband ocean-bottom-seismometer (BBOBS) deployment designed to investigate multiscale convection beneath the Pacific plate through passive source seismology. This project is a collaborative research effort led by investigators at Northern Arizona University (Gaherty), the University of California Santa Barbara (Eilon), Brown University (Forsyth), and Columbia University (Ekström). The experiment utilized broadband OBSs developed and operated by the Scripps Institution of Oceanography (SIO) OBS lab, and all research cruises were conducted aboard University-National Oceanographic Laboratory System vessels. The goals of the experiment include: 3D seismic imaging of the mantle lithosphere and asthenosphere; measurement of seismic anisotropy beneath and within the ocean plate; expanding the coverage of ocean-traversing ray paths for global seismology; and evaluation of ocean plate ageing and maturation.

The experiment comprises two 30-instrument BBOBS arrays deployed for ~13 months each across two ~500 × 500 km regions of Pacific seafloor, with approximate crustal ages of 40 Ma ("Young ORCA," 2018–2019) and 120 Ma ("Old ORCA," 2019–2020) (Fig. 1). The primary data yielded by this experiment are broadband three-component seismic and one-component differential pressure data collected continuously for the deployment durations. This project is a US contribution to the international Pacific Array of Arrays (Kawakatsu *et al.*, 2019) and thus targets locations far from existing seismic stations, and ocean plate ages distinct from those previously covered by a focused BBOBS deployment. The specific sites were also chosen as regions where lineations are observed in the gravity field (Haxby and Weissel, 1986), including modern Seasat-derived compilations (Sandwell *et al.*, 2014). These gravity lineations, which align approximately with absolute plate motion, have a wavelength of ~200 km and have been variously associated with small-scale subplate convective "Richter" rolls (Buck and Parmentier, 1986), lithospheric cracking (Sandwell and Fialko, 2004), or subplate flow of "hot fingers" (Weeraratne *et al.*, 2003; Ballmer *et al.*, 2009). These alternative hypotheses can be discriminated through detailed imaging of the oceanic lithosphere and asthenosphere, and comparison with detailed seafloor maps, including seamount locations. We collected a secondary dataset of high-resolution multibeam swath bathymetry maps across both array footprints. The age and nature of seamount volcanism within these areas also has the potential to inform our understanding of oceanic plate maturation and subplate convection, and so we dredged several seamounts within and adjacent to the array footprints for geochemical analysis by

1. University of California Santa Barbara, Santa Barbara, California, U.S.A., https://orcid.org/0000-0002-4373-646X (ZCE); 2. Northern Arizona University, Flagstaff, Arizona, U.S.A., https://orcid.org/0000-0003-2513-5510 (JBG); 3. Department of Earth, Environmental and Planetary Sciences, Brown University, Providence, Rhode Island, U.S.A., https://orcid.org/0000-0003-3251-2919 (JR); https://orcid.org/0000-0003-1450-2143 (DWF); 4. Institute of Geophysics and Planetary Physics, Scripps Institution of Oceanography, San Diego, California, U.S.A.; 5. Lamont Doherty Earth Observatory of Columbia University, Palisades, New York, U.S.A.

*Corresponding author: eilon@ucsb.edu

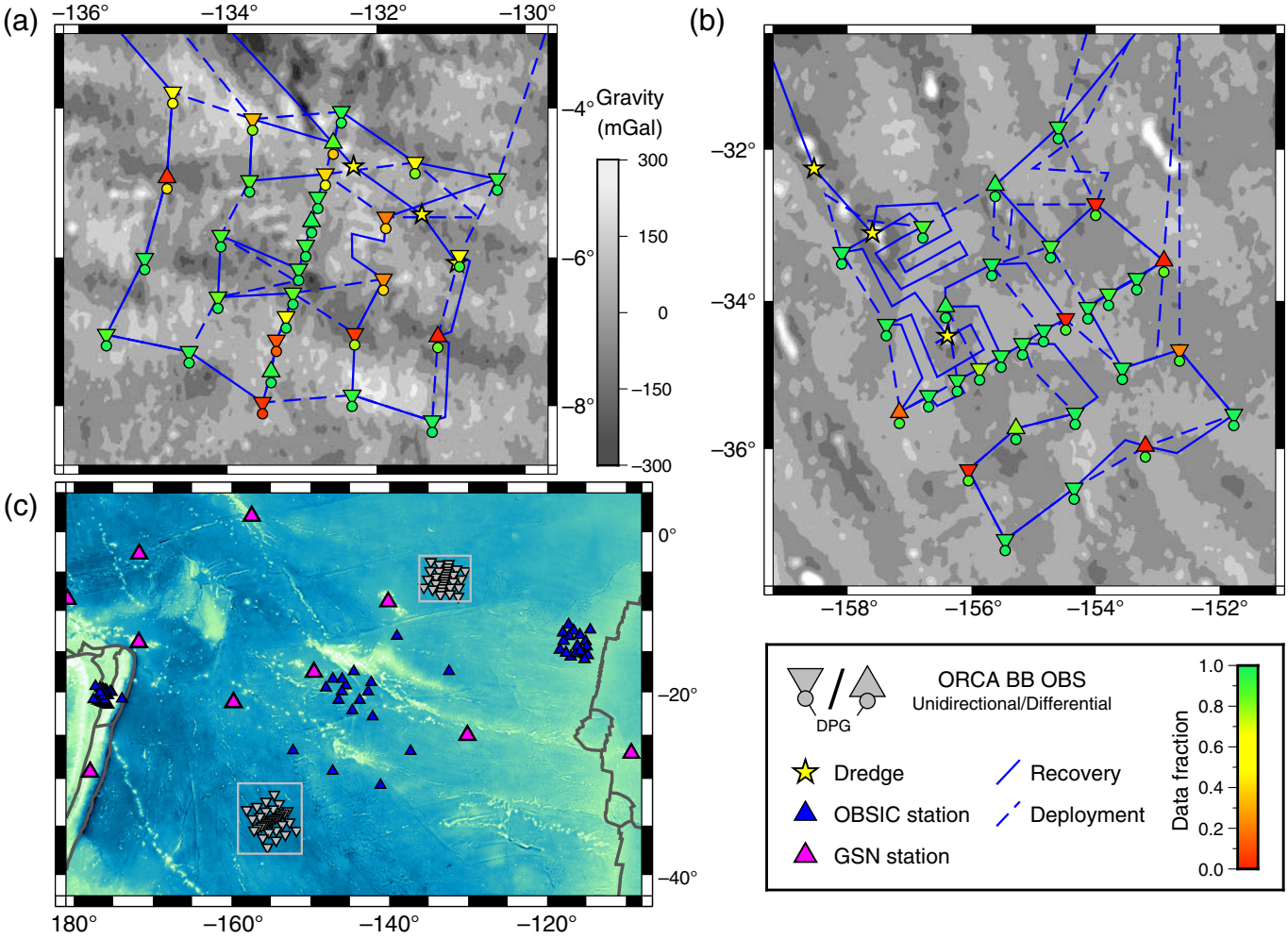

Figure 1. Map of stations in ocean-bottom seismometer (OBS) Research into Convecting Asthenosphere (ORCA) experiment, showing both array configurations and overall station data quality. (a) Young ORCA stations (triangle and circle symbols) and dredge locations (yellow stars) superimposed on Seasat-derived free air gravity anomaly (Sandwell *et al.*, 2014) that has been filtered in the 2D wavenumber domain between 300 and 400 km. Tracks of deployment (dashed blue) and recovery (solid blue) cruises shown. (b) As for (a) but for Old ORCA. (c) Southern Pacific with all broadband seismic stations shown, including previous OBSIC (GLIMPSE, Lau basin) and Japanese (PLUME, TIARES) OBS experiments in blue, GSN stations on islands (magenta), and ORCA stations (gray). The background is the ETOPO1 global relief model (National Oceanic and Atmospheric Administration [NOAA] National Geophysical Data Center, 2009). ORCA station icons are colored to display the fraction of total (13 months) data on seismic components (triangles, in which 100% corresponds to 39 months of usable data total, summed across the three components) and differential pressure gauge (DPG) instruments (circles). The color version of this figure is available only in the electronic edition.

collaborator Matthew Jackson at UC Santa Barbara. This experiment yielded one of the largest and the most complete OBS datasets recorded in the Pacific Ocean to date, bringing broadband seismic coverage to new areas of the planet, driving forward our understanding of the ocean plates.

Deployments

Two OBS arrays, termed "Young ORCA" and "Old ORCA", were deployed diachronously for this experiment. Both comprised 30 SIO broadband instruments, each equipped with Trillium T-240 three-component seismometers and an SIO-built differential pressure gauges (DPGs) (Cox *et al.*, 1984). The data were recorded by SIO-built digitizers at a sample rate of 50 Hz. Most of the seismometers operated in single-ended mode (range 0–2.5 V), but a small subset in each array operated in differential mode (range ±2.5 V). All seismometers operated in a right-handed system, so seismic channels CH0, CH1, and CH2 correspond to BH2, BH1, and BHZ, respectively, in which BH2 (nominal east) is 90° clockwise of BH1 (nominal north). Horizontal orientations, where known, are given in Table 1 and Table S1, available in the supplemental material to this article. Channel CH3 corresponded to the DPG, BDH. The details of the two array deployments and recoveries are given subsequently. On all cruises, underway data were collected, providing a collocated dataset of gravity measurements. The locations and deployment timing of all

TABLE 1
Station Parameters for All Sites in the ORCA Experiment

Station Code	Network	On Date (yyyy/mm/dd)	Off Date (yyyy/mm/dd)	Latitude (°)	Longitude (°)	Elevation (m)	Orientation (°)
EE01	YoungORCA	2018/04/16	2019/05/15	–4.947	–130.3814	–4653	84.9
EE02	YoungORCA	2018/04/16	2019/04/09	–5.9764	–130.8896	–4641	9.8
EE03	YoungORCA	2018/04/17	2019/03/12	–7.0644	–131.1788	–4637	NaN
EE04	YoungORCA	2018/04/17	2019/05/27	–8.2043	–131.2551	–4693	24.8
EC01	YoungORCA	2018/04/23	2019/03/09	–4.7261	–131.4852	–4590	109.8
EC02	YoungORCA	2018/04/22	2018/09/27	–5.462	–131.8769	–4763	NaN
EC03	YoungORCA	2018/04/20	2018/10/10	–6.2916	–131.9104	–4733	NaN
EC04	YoungORCA	2018/04/20	2019/02/16	–7.0275	–132.2942	–4768	NaN
EC05	YoungORCA	2018/04/18	2019/05/17	–7.8562	–132.3298	–4595	36.4
CC01	YoungORCA	2018/04/24	2019/05/24	–4.0458	–132.4745	–4757	330.4
CC02	YoungORCA	2018/04/24	2019/05/24	–4.4646	–132.583	–4457	90.5
CC03	YoungORCA	2018/04/24	2019/01/30	–4.8816	–132.6889	–4730	122.6
CC04	YoungORCA	2018/04/22	2019/05/22	–5.1937	–132.79	–4603	357.2
CC05	YoungORCA	2018/04/21	2019/05/22	–5.5174	–132.873	–4788	121.2
CC06	YoungORCA	2018/04/21	2019/05/22	–5.8385	–132.9518	–4812	52.8
CC07	YoungORCA	2018/04/21	2019/05/21	–6.1588	–133.0464	–4617	108.2
CC08	YoungORCA	2018/04/19	2019/05/20	–6.4817	–133.1233	–4755	150.3
CC09	YoungORCA	2018/04/19	2019/05/18	–6.7994	–133.2164	–4606	54.4
CC10	YoungORCA	2018/04/19	2018/06/09	–7.1148	–133.3457	–4609	NaN
CC11	YoungORCA	2018/04/19	2019/05/19	–7.5368	–133.4166	–4625	224.5
CC12	YoungORCA	2018/04/18	2018/05/07	–7.9545	–133.5322	–4586	120.3
WC01	YoungORCA	2018/04/25	2019/03/06	–4.1433	–133.6649	–4497	NaN
WC02	YoungORCA	2018/04/25	2019/05/23	–4.9726	–133.7054	–4629	29.8
WC03	YoungORCA	2018/04/26	2019/05/21	–5.7077	–134.0913	–4471	125.7
WC04	YoungORCA	2018/04/26	2019/05/21	–6.5352	–134.1305	–4544	121.3
WC05	YoungORCA	2018/04/27	2019/05/19	–7.2694	–134.5177	–4489	103.5
WW01	YoungORCA	2018/04/29	2019/01/05	–3.7852	–134.737	–4546	294.6
WW02	YoungORCA	2018/04/28	2018/10/12	–4.9283	–134.8136	–4673	NaN
WW03	YoungORCA	2018/04/28	2019/05/18	–6.0155	–135.112	–4399	303.1
WW04	YoungORCA	2018/04/27	2019/05/18	–7.0385	–135.6272	–4477	257.6
NN01	OldORCA	2019/11/16	2020/11/20	–31.7096	–154.6033	–5050	345.9
NN02	OldORCA	2019/11/30	2020/11/21	–32.4648	–155.6196	–5280	70.5
NN03	OldORCA	2019/11/29	2020/12/03	–33.0141	–156.7863	–5041	250.1
NN04	OldORCA	2019/11/28	2020/12/02	–33.3572	–158.0949	–5224	92.8

On date refers to deployment date, off date refers either recovery date or date on which main batteries died, if earlier; latitude, longitude, and elevation from OBSrange survey result; orientation azimuth of CH1 (also known as BH1) channel, where known. For uncertainties in station orientations, see supplemental material. ORCA, ocean-bottom seismometer (OBS) Research into Convecting Asthenosphere.
(Continued next page.)

TABLE 1 (continued)
Station Parameters for All Sites in the ORCA Experiment

Station Code	Network	On Date (yyyy/mm/dd)	Off Date (yyyy/mm/dd)	Latitude (°)	Longitude (°)	Elevation (m)	Orientation (°)
NM01	OldORCA	2019/11/16	2020/10/07	−32.7147	−154.0008	−5178	NaN
NM02	OldORCA	2019/11/18	2020/11/21	−33.2745	−154.7265	−5003	229.3
NM03	OldORCA	2019/11/18	2020/11/28	−33.5136	−155.6739	−5046	223.3
NM04	OldORCA	2019/11/26	2020/11/28	−34.0765	−156.4188	−5353	109.2
NM05	OldORCA	2019/11/27	2020/11/30	−34.3171	−157.377	−5427	76.3
MM01	OldORCA	2019/11/17	2020/09/28	−33.4654	−152.9011	−5173	NaN
MM02	OldORCA	2019/11/17	2020/11/22	−33.7024	−153.3388	−5159	145.2
MM03	OldORCA	2019/11/17	2020/11/22	−33.9104	−153.7923	−5141	287.5
MM04	OldORCA	2019/11/18	2020/11/23	−34.0909	−154.1255	−5118	16.9
MM05	OldORCA	2019/11/20	2020/10/15	−34.2402	−154.4836	−5083	NaN
MM06	OldORCA	2019/11/19	2020/11/27	−34.397	−154.8403	−5202	171.6
MM07	OldORCA	2019/11/25	2020/11/27	−34.574	−155.1795	−5361	216.7
MM08	OldORCA	2019/11/26	2020/11/28	−34.7401	−155.5257	−5450	120.2
MM09	OldORCA	2019/11/26	2020/11/29	−34.9139	−155.8709	−5307	159
MM10	OldORCA	2019/11/27	2020/11/29	−35.0689	−156.2322	−5419	241.4
MM11	OldORCA	2019/11/27	2020/11/29	−35.2787	−156.6947	−5408	207.5
MM12	OldORCA	2019/11/27	2020/11/03	−35.5034	−157.1648	−5293	NaN
SM01	OldORCA	2019/11/22	2020/10/19	−34.6578	−152.6489	−5358	NaN
SM02	OldORCA	2019/11/20	2020/11/23	−34.9065	−153.5697	−5348	216.1
SM03	OldORCA	2019/11/25	2020/11/26	−35.5163	−154.3313	−5339	22.8
SM04	OldORCA	2019/11/25	2020/11/26	−35.7224	−155.2847	−5352	124.3
SM05	OldORCA	2019/11/24	2020/10/10	−36.2893	−156.0514	−5344	NaN
SS01	OldORCA	2019/11/23	2020/11/24	−35.5327	−151.7736	−5323	36
SS02	OldORCA	2019/11/23	2020/10/31	−35.9625	−153.1993	−5423	NaN
SS03	OldORCA	2019/11/24	2020/11/25	−36.5422	−154.3482	−5314	104.9
SS04	OldORCA	2019/11/24	2020/11/25	−37.2546	−155.4594	−5243	348.7

On date refers to deployment date, off date refers either recovery date or date on which main batteries died, if earlier; latitude, longitude, and elevation from OBSrange survey result; orientation azimuth of CH1 (also known as BH1) channel, where known. For uncertainties in station orientations, see supplemental material. ORCA, ocean-bottom seismometer (OBS) Research into Convecting Asthenosphere.

stations in the arrays are given in Table 1. The science parties spanning all four cruises included 30 early career scientists from 20 institutions, including five assistant professors (or non-US equivalent), two postdoctoral scholars, and 23 graduate students (Fig. 2).

Young ORCA Array

This array was deployed from the R/V Kilo Moana (KM), cruise ID KM1807, departing San Diego, California, 7 April 2018 and arriving in Honolulu, Hawaii, 7 May 2018. The array, situated in the equatorial Pacific northeast of the Marquesas Islands, spanned a region approximately between (8° S, 146° W) and (4° S, 130° W) (Fig. 1). Seafloor age beneath the array ranges from ~40 to 45 Ma (Müller *et al.*, 2008), and the bounding fracture zones establish a fossil seafloor-spreading direction of ~75° azimuth. Spreading rates appear to be very fast, with half-rates of order 100–120 mm/yr (Müller *et al.*, 2008). The array comprised a dense 450 km long line of 12 stations at an azimuth of 015°, with two sparser outer lines of five and four stations offset to either side of the main line by ~115 km and ~220 km,

Figure 2. Fieldwork photos from deployment and recovery of both arrays. Center figure: Scripps Institution of Oceanography (SIO) OBS on back deck of R/V Kilo Moana prior to Old ORCA deployment. Clockwise from top left: Science party conducts fire drill on back deck of R/V Roger Revelle during Old ORCA recovery; disassembly of Old ORCA instrument following recovery; tag lines being affixed to sensor ball during Old ORCA recovery; students and SIO OBS tech communicating with Old ORCA instrument during postdeployment acoustic survey using EdgeTech 8011M deck box connected to hull-mounted 12 kHz transducer; student and PI issuing burn command to release instrument during Old ORCA recovery; young ORCA instrument deployment from A-frame of R/V Kilo Moana for Young Orca array. Photo credits: H. Janiszewski, E. Nathan, and Z. Eilon. The color version of this figure is available only in the electronic edition.

respectively. The configuration of this array was designed to provide sufficient aperture for recording long-period surface waves, and sufficient density and aperture for upper mantle body wave tomography. The dense central line was aligned roughly perpendicular to the azimuth of gravity lineations in this region. The first instrument (EE01) was deployed on 16 April 2018 UTC and the last (WC01) on 29 April 2018 UTC. Precise seafloor instrument locations were determined through an acoustic ranging survey, using a survey pattern that contained both radial and circular arc components and a ~0.7 NM aperture, solving for station coordinates using the OBSrange software (developed during this cruise; Russell *et al.*, 2019). Throughout the expedition, we mapped bathymetry using the KM's Simrad EM122 12 kHz swath sonar system, sailing at ~8 kt for the interstation mapping legs. We cleaned the ping data on board using QPS Qimera processing software.

This OBS array had approximately 13 months of nominal recording time. OBSs were recovered using the R/V Kilo Moana, cruise ID KM1908, sailing in and out of Honolulu, Hawaii, from 8 May to 6 June 2019. The first instrument (WW01) was recovered on 16 May 2019 UTC and the last (EE02) on 27 May 2019 UTC. All 30 instruments were successfully recovered. This recovery cruise also included three dredges, recovering a good seafloor basalt sample at one site (Fig. 1). During the recovery cruise, we used the same multibeam sonar mapping and processing procedures, adjusting interstation tracks to add new, nonoverlapping swaths of mapped seafloor, and collected additional data of interest to utilize excess contingency time.

Old ORCA Array

This array was deployed from the R/V Kilo Moana (KM), cruise ID KM1922, sailing in and out of Pape'ete, French Polynesia, from 12 November to 5 December 2019. The array, situated in the southwest Pacific, south of French Polynesia and east of New Zealand, spanned a region approximately between (38° S, 158° W) and (32° S, 152° W) (Fig. 1). The array sits on ancient oceanic crust formed at a failed spreading ridge now identified as the Osborn trough (26.25° S, 168° W), with crustal age ranging from ~115 to 135 Ma (Müller *et al.*, 2008). Discontinuous transitions to ocean crust formed at ridges corresponding to the modern-day East-Pacific Rise and Pacific-Antarctic ridge lie approximately 300 km east and south of the array perimeter. The dominant direction of abyssal hill fabric observed in high-resolution bathymetry (Ryan *et al.*, 2009) suggests a fossil seafloor-spreading direction of ~340° azimuth. This inferred spreading direction is roughly consistent with the age model of Müller *et al.* (2008), and the associated half-spreading rate is inferred to be intermediate (~30 mm/yr). The abyssal-hill fabric and associated spreading direction are inconsistent with the spreading direction predicted for this site using a more recent age model (Seton *et al.*, 2020), and we prefer the Müller *et al.* (2008) model for this region.

The configuration of this array was identical to the Young ORCA array, but with the central line orientated at 060°, perpendicular to the local gravity lineaments. The first instrument (NN01) was deployed on 16 November 2019 UTC, and the last (NN02) on 30 November 2019 UTC. Again, seafloor instrument locations were determined by acoustic ranging survey and the OBSrange package, using the same survey pattern as YoungORCA but with a 0.5 NM aperture. During this cruise, we mapped bathymetry using the KM's Simrad EM122 12 kHz swath sonar system, sailing at ~8 kt for the mapping legs. The Old ORCA footprint overlaps the 2007 MGLN13MV multibeam mapping experiment (see Data and Resources), which covered the southern third of our array area in detail; our new mapping efforts focused on the northern part of the array. We cleaned the ping data on board using QPS Qimera processing software.

The OBS array had approximately 13 months of nominal recording time. OBSs were recovered on the R/V Roger Revelle, cruise ID RR2003, departing San Diego, California, 3 November 2020 and arriving in Honolulu, Hawaii, 20 December 2020. Because of the Covid-19 pandemic, all participants in the recovery cruise were strictly quarantined for at least 14 days prior to boarding, accompanied by testing regimen. On board, strict social distancing and hygiene protocols were followed (Fig. 2). The first instrument (NN01) was recovered on 19 November 2020 UTC and the last (NN03) on 2 December 2020 UTC. All 30 instruments were successfully recovered. This recovery cruise also included three dredges of seamounts within and adjacent to the Old ORCA footprint, with recovery of usable samples at all sites (Fig. 1). During the recovery cruise, we mapped bathymetry using the RR's Simrad EM124 12 kHz swath sonar system, sailing at ~8 kt while mapping new swaths of seafloor not covered by previous cruises. We processed the multibeam data on board and following the experiment using QPS Qimera2 software.

Data Quality and Availability

We describe the data quality of the two deployments (Young ORCA and Old ORCA) separately, in the text below. Table 2 summarizes the data quality at each station. Supplemental materials F1 and F2 contain probability density functions for power spectral densities of stations in Young ORCA and Old ORCA, respectively, and F3 and F4 contain spectrograms for the deployment durations of the same.

Young ORCA

This array yielded approximately 68% usable data recovery, measured as a fraction of a nominal 13-month deployment period over which waveforms may exist on all channels. Separated by data type, 64% of seismic data and 80% of DPG data were recovered. Unfortunately, not all of these data are high quality or necessarily usable. Numerous instrument problems impacted this experiment: (1) several stations were recovered with depleted main batteries and recorded data for less than the full deployment duration; (2) of these stations, several also had depleted clock batteries, meaning no on board time drift could be computed; (3) several stations recorded unusual spectral noise peaks, had above-average long-period noise levels, and experienced numerous data gaps; (4) several of the stations experienced failures of their SanDisk 64 GB compact flash data cards, requiring forensic data recovery that yielded incomplete records. This constellation of issues (certainly 1–3) likely stemmed from a sensor-release failure. SIO BBOBS are deployed with the seismic sensor suspended from an arm that protrudes from the main body of the instrument, with an Mg-pin corrosion release mechanism designed to drop the sensor onto the seafloor 24–48 hr after deployment. The release mechanism for the OBSs was redesigned for this experiment to take the Mg pins out of the load path due to safety concerns with the previous design, but did not function as expected. Several instruments appear to have remained hanging on the arm for months of time and in some cases likely for the entire deployment. The SIO OBSs do not record a drop status; our inference of drop failures and drop times is based on distinct patterns of data noise, and, in the case of some stations, a step-wise change in spectral properties before versus after a certain date.

We computed hourly velocity power spectra and deployment spectrograms for all stations to determine data quality and noise characteristics (Fig. 3, supplemental materials F3, F4). Systematics in the mean, maximum and minimum, and range of the power spectra allow efficient classification of channel performance and data anomalies. Distinct spectral patterns

TABLE 2
Station Data Quality and Health for All Sites in the ORCA Experiment

Station Code	Duration (Days)	Battery Status	Data Card	Drop%	Drop Date (yyyy/mm/dd)	Seismic Data	DPG Data
EE01	394	Ok	Failed	68%	2018/08/20	94%	99%
EE02	358	Dead	Ok	66%	2018/08/15	66%	90%
EE03	329	Dead	Ok	100%	2018/04/17	0%	82%
EE04	405	Ok	Ok	57%	2018/10/08	98%	102%
EC01	320	Dead	Failed	0%	2019/03/09	48%	81%
EC02	158	Dead	Ok	100%	2018/04/22	20%	39%
EC03	173	Dead	Failed	100%	2018/04/20	23%	40%
EC04	302	Dead	Ok	100%	2018/04/20	5%	76%
EC05	394	Ok	Failed	50%	2018/11/02	94%	97%
CC01	395	Ok	Failed	100%	2018/04/24	95%	97%
CC02	395	Ok	Ok	64%	2018/09/15	86%	36%
CC03	281	Dead	Failed	43%	2018/10/01	39%	68%
CC04	395	Ok	Ok	100%	2018/04/22	96%	100%
CC05	396	Ok	Ok	100%	2018/04/21	98%	100%
CC06	396	Ok	Ok	52%	2018/10/26	92%	100%
CC07	395	Ok	Ok	45%	2018/11/22	93%	100%
CC08	396	Ok	Ok	40%	2018/12/10	85%	100%
CC09	394	Ok	Failed	100%	2018/04/19	50%	99%
CC10	51	Ok	Failed	100%	2018/04/19	12%	13%
CC11	395	Ok	Ok	100%	2018/04/19	94%	100%
CC12	19	Ok	Failed	100%	2018/04/18	5%	5%
WC01	315	Dead	Ok	100%	2018/04/25	33%	79%
WC02	393	Ok	Failed	64%	2018/09/15	86%	98%
WC03	390	Ok	Ok	69%	2018/08/23	89%	99%
WC04	390	Ok	Ok	58%	2018/10/05	83%	98%
WC05	387	Ok	Ok	42%	2018/12/06	95%	98%
WW01	251	Ok	Failed	0%	2019/01/05	64%	64%
WW02	167	Dead	Ok	100%	2018/04/28	3%	42%
WW03	385	Ok	Ok	0%	2019/05/18	97%	98%
WW04	386	Ok	Failed	51%	2018/11/01	86%	98%
NN01	370	Ok	Ok	100%	2019/11/16	96%	100%
NN02	357	Ok	Ok	100%	2019/11/30	96%	96%

Columns are station code; duration (in days) for which the station returned data; main battery status upon recovery; flash memory data card status upon recovery (sites with "failed" data cards had their data retrieved through a forensic data recovery process); fraction of the deployment for which the seismic sensors were dropped from the arm (100% corresponds to dropped throughout, 0% corresponds to hanging throughout); approximate date (±3 days for mid-deployment drops) on which seismic sensor dropped from the arm; seismic data recovery rate, measured as a fraction of the data classified as "normal" divided by the total potential three-component data for the 80th percentile deployment duration (13 months for Young ORCA, 12.2 months for Old ORCA). For instance, a seismic sensor that operated for the full duration but with one channel broken would get a value of 67%; differential pressure gauge (DPG) data recovery rate, as for seismic data but only for the single pressure channel.
(Continued next page.)

TABLE 2 (continued)
Station Data Quality and Health for All Sites in the ORCA Experiment

Station Code	Duration (Days)	Battery Status	Data Card	Drop%	Drop Date (yyyy/mm/dd)	Seismic Data	DPG Data
NN03	370	Ok	Ok	100%	2019/11/29	90%	100%
NN04	370	Ok	Ok	100%	2019/11/28	99%	100%
NM01	326	Dead	Ok	100%	2019/11/16	0%	88%
NM02	369	Ok	Ok	100%	2019/11/18	90%	100%
NM03	376	Ok	Ok	100%	2019/11/18	99%	101%
NM04	368	Ok	Ok	100%	2019/11/26	95%	99%
NM05	369	Ok	Ok	100%	2019/11/27	96%	100%
MM01	316	Dead	Ok	100%	2019/11/17	0%	85%
MM02	371	Ok	Ok	100%	2019/11/17	98%	100%
MM03	371	Ok	Ok	100%	2019/11/17	90%	100%
MM04	371	Ok	Ok	100%	2019/11/18	98%	100%
MM05	330	Dead	Ok	100%	2019/11/20	0%	89%
MM06	374	Ok	Ok	100%	2019/11/19	100%	101%
MM07	368	Ok	Ok	100%	2019/11/25	95%	99%
MM08	368	Ok	Ok	100%	2019/11/26	95%	100%
MM09	369	Ok	Ok	100%	2019/11/26	77%	100%
MM10	368	Ok	Ok	100%	2019/11/27	96%	100%
MM11	368	Ok	Ok	100%	2019/11/27	99%	100%
MM12	342	Dead	Ok	100%	2019/11/27	16%	92%
SM01	332	Dead	Ok	100%	2019/11/22	22%	90%
SM02	369	Ok	Ok	100%	2019/11/20	99%	100%
SM03	367	Ok	Ok	100%	2019/11/25	98%	99%
SM04	367	Ok	Ok	100%	2019/11/25	80%	99%
SM05	321	Dead	Ok	100%	2019/11/24	1%	86%
SS01	367	Ok	Ok	100%	2019/11/23	98%	99%
SS02	343	Dead	Ok	100%	2019/11/23	0%	92%
SS03	367	Ok	Ok	100%	2019/11/24	98%	99%
SS04	367	Ok	Ok	100%	2019/11/24	97%	99%

Columns are station code; duration (in days) for which the station returned data; main battery status upon recovery; flash memory data card status upon recovery (sites with "failed" data cards had their data retrieved through a forensic data recovery process); fraction of the deployment for which the seismic sensors were dropped from the arm (100% corresponds to dropped throughout, 0% corresponds to hanging throughout); approximate date (±3 days for mid-deployment drops) on which seismic sensor dropped from the arm; seismic data recovery rate, measured as a fraction of the data classified as "normal" divided by the total potential three-component data for the 80th percentile deployment duration (13 months for Young ORCA, 12.2 months for Old ORCA). For instance, a seismic sensor that operated for the full duration but with one channel broken would get a value of 67%; differential pressure gauge (DPG) data recovery rate, as for seismic data but only for the single pressure channel.

prior to the apparent drop time include: (a) A noise peak at 1.5–2 Hz (which seems to migrate to fractionally higher frequencies over the first few months of the deployment) that we attribute to a resonant vibration of the sensor on the arm; (b) regular multiday data gaps or railed sensor values, which we attribute to weekly gimbal leveling cycles; (c) extremely noisy horizontal components, particularly in the bottom current frequency band (<0.1 Hz); (d) low vertical-pressure coherence and high vertical-horizontal coherence. Drop times were estimated on the basis of abrupt transitions from these noise

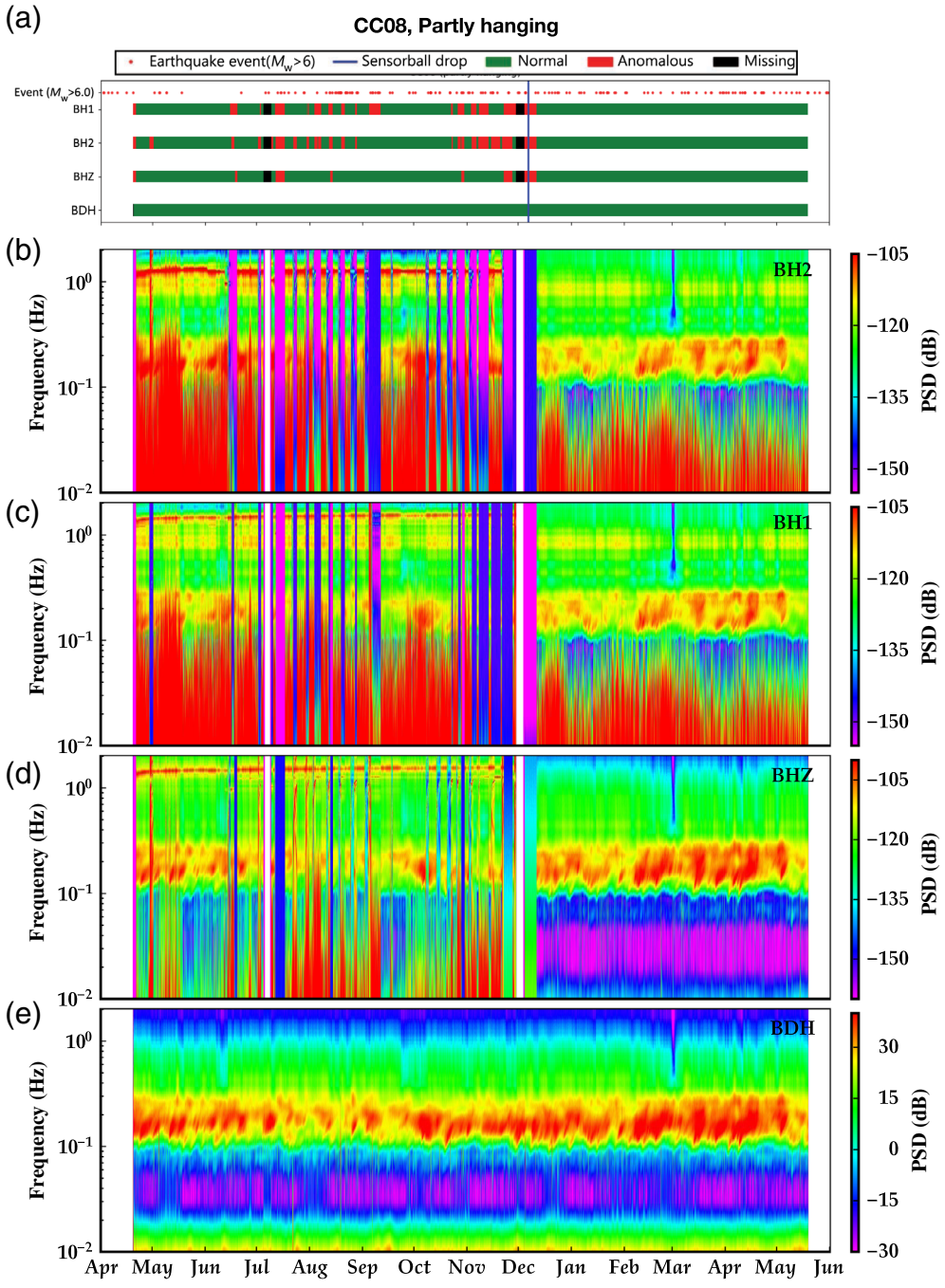

Figure 3. Example of data classification and four-component spectrograms for Young ORCA station CC08 (deployed April 2018–May 2019). (a) Data quality status for all four instrument channels. (b–e) Spectrograms for BH2, BH1, BHZ, and BDH components. Units for the seismic channels are relative to 1 (m/s)/Hz and for the pressure channel 1 Pa/Hz. The seismic channels for this station show several hallmarks of a hanging seismic sensor for a large fraction (~60%) of the deployment time: frequent data gaps, high long-period noise levels, particularly on horizontal components, and a ~1.5 Hz spectral peak. These features all abruptly cease in December 2018, when we estimate the seismic sensor dropped. The DPG is unaffected by the hanging throughout. Note that data classified as "Normal" includes the predrop time; this data are partly usable, with caution. The color version of this figure is available only in the electronic edition.

characteristics to those typical for deep-water OBS deployments (e.g., Webb, 1998; Janiszewski *et al.*, 2020), and are recorded in the station data table. Remarkably, the vertical-component data are usable for some portion of the hanging time as vertical ground motion is transmitted through the water and/or the body of the instrument, but we strongly caution against using any horizontal data prior to the sensor drop time, as horizontal currents and resonance effects dominate. The DPG sensor is attached to the main body of the instrument and unaffected by the seismometer drop status. No instruments surfaced with sensors are still on the arm. We speculate that sensors that may have been hanging immediately prior to recovery were knocked loose during the seafloor release and ascent.

Twenty-one of 30 instruments were recovered with still-operational data loggers. Main battery depletion resulted in shutdown of data loggers for the other nine instruments; of these instruments, eight also had depleted Seascan backup clock batteries, meaning it was not possible to determine and correct for clock drift directly. For these stations, we determined clock drift using ambient noise cross correlation (ANCC), assuming stationarity of the cross correlogram (Stehly *et al.*, 2007; Gouédard *et al.*, 2014; Hannemann *et al.*, 2014; Hable *et al.*, 2018). We used daily ambient noise cross-correlation functions (CCFs) filtered from 3 to 8 s to estimate clock drift relative to a 30-day reference CCF stack, comparing stations with unknown timing to those with corrected times.

Because of the noise on seismometer channels for hanging stations (see earlier), we used the pressure channels to determine clock drift, but the datalogger drift rates applies to all channels. This technique revealed roughly linear clock drifts (Figs. S1 and S2), validating the assumption of constant drift used to time-correct OBSs with functional clocks, which is based on a linear interpolation from the time error logged at recovery. Although we computed daily drifts, we used the best-fitting linear drift rate at each station to correct the final data. Averaging across time drifts determined directly from the Seascan clocks and the ANCC results, the median absolute drift was 1.896 ms/day.

Old ORCA

The data recovery for this component of the experiment was very good. Measured as a fraction of the deployment period for which waveforms exist on all channels for a nominal 12.2 month deployment, this array yielded 80% usable data recovery. That average corresponds to 74% of seismic data, and 97% of DPG data. Twenty-three of 30 stations were recovered with fully-functional data loggers (i.e., nondepleted batteries), with >12 months of high-quality data on seismic and pressure channels. One (NN02) of these 23 stations had anomalously noisy horizontal channels. The other seven stations (Fig. 1; Table 2) had depleted batteries and nonfunctional dataloggers upon recovery. All seven of these stations turned out to have unusable seismic channels, but the majority had ∼11 months of good DPG data. We speculate that the seismic sensors were somehow out of level for all these stations, as the channel values indicate masses sitting on the rails. The excess power draw from railed masses (as well as the smaller power draw from weekly leveling cycles) caused premature depletion of the instrument batteries, shutting down the datalogger a month or two prior to recovery. All 30 of the stations were recovered with working Seascan clocks, enabling internal clock drift times to be calculated and the corresponding data corrections made. Most clock drifts were within manufacturer spec, and the mean absolute drift rate was 1.312 ms/day.

Data Quality Categorization and Features for Both Arrays

Based on the amplitude spectrograms of daily files, we categorize daily station quality as "normal," "anomalous," or "missing" for each channel. "Normal" indicates good data in keeping with expectations for the instrument type and the relevant noise environment. "Anomalous" indicates that data are present, but that the shape or height of the spectrum is very unusual; these days are unlikely to offer usable data. "Missing" indicates days for which data are wholly absent, zeroed, or a constant value (e.g., for a fully railed sensor). Anomalous data were identified as that with a mean amplitude spectral value below 40 dB (prior to instrument response removal, for consistent treatment of seismic and pressure channels), or a standard deviation (i.e., amplitude variation across frequencies) lower than 7.5 dB; these values were chosen specifically for this noise environment and instrument type. To assist users of this dataset, we include two supplemental materials with this article that describe the data state according to this rubric for all channels for the deployment duration of all ORCA stations (normal is coded as 2, anomalous as 1, and missing as 0) for both Young ORCA (supplemental material 5) and Old ORCA (supplemental material 6) arrays. Figure S4 shows the span of each station's data quality throughout the experiment windows, with global $M_w > 6.0$ teleseismic earthquake occurrences (from the International Federation of Digital Seismograph Networks global catalog) plotted for reference. For stations where we infer a delayed release of the seismometer from the instrument arm, this plot also indicates estimated release times. The data recovery numbers cited in the previous sections refer to the "normal" data only, but we caution users that not all of this data are equally useful. The Young ORCA data, in particular, include time periods in which spectra are unusual or diagnostic of hanging instruments but not abnormal enough to be classified as "anomalous."

The seismic data from this experiment are currently available from the Incorporated Research Institutions for Seismology Data Management Center (DMC), under network code XE. The DMC also houses instrument response files. Users should note that 11 of the total stations (six for Young ORCA and five for Old ORCA) had differential seismic sensors (output range ±2.5 V), and the rest were single-ended sensors (output range 0–2.5 V) with accordingly distinct gain values (example response files for each sensor configuration are included as supplemental material 7). For stations with two "normal" horizontal channels available, orientation of the OBS sensors was computed (see the Initial Results section) and is contained in the supplemental material of this article.

Multibeam Data

The raw MultiBeam swath bathymetry data collected on all deployment and recovery legs is (or will shortly be) available via the Rolling Deck to Repository (R2R) portal under the respective cruise IDs (see Data and Resources). R2R also houses ancillary processed underway data, of which the relevant geophysical datasets are those from the gravimeter and magnetometer (the latter is not available for Young ORCA). Processed MultiBeam surface files are housed on the Dryad data repository, and merged netCDF grids of the Young ORCA site (100, 125, and 200 m sampling) are available on R2R (see Data and Resources). Processed and gridded data are also available by request from the investigators. The quality of the processed data is excellent, with mean resolution estimated at 20 m in the vertical and <100 m in the horizontal dimensions. Low-resolution examples of the multibeam surface for the two ORCA footprints are shown in Figure 4.

Initial Observations

Power spectral probability density functions (incorporating only "normal" days) were computed for all channels and all

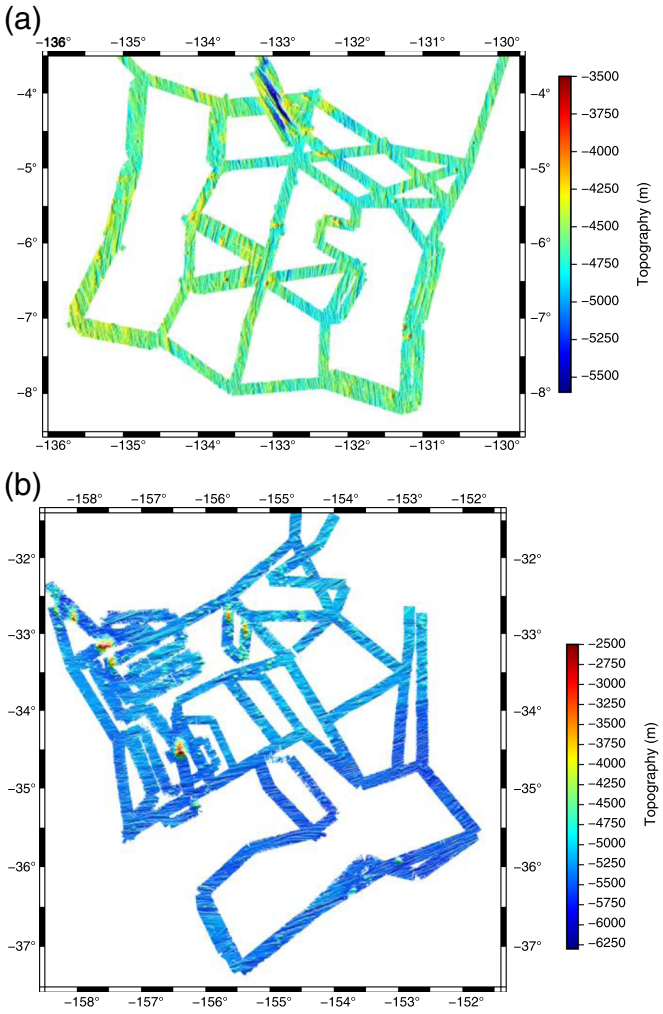

Figure 4. Multibeam dynamic surface for the (a) Young ORCA and (b) Old ORCA footprints. This data were collected as raw.kall and.kmall Kongsberg files and processed using Qimera ping-editing software to remove anomalous points, after which a smooth dynamic surface was fitted. This figure is a down-sampled, low-resolution version of the actual surface file. Evident features include (previously unmapped) seamounts, clear abyssal hill fabric with long-fault scarps, small truncated-cone features with low relief, and long-wavelength bathymetric variation. The color version of this figure is available only in the electronic edition.

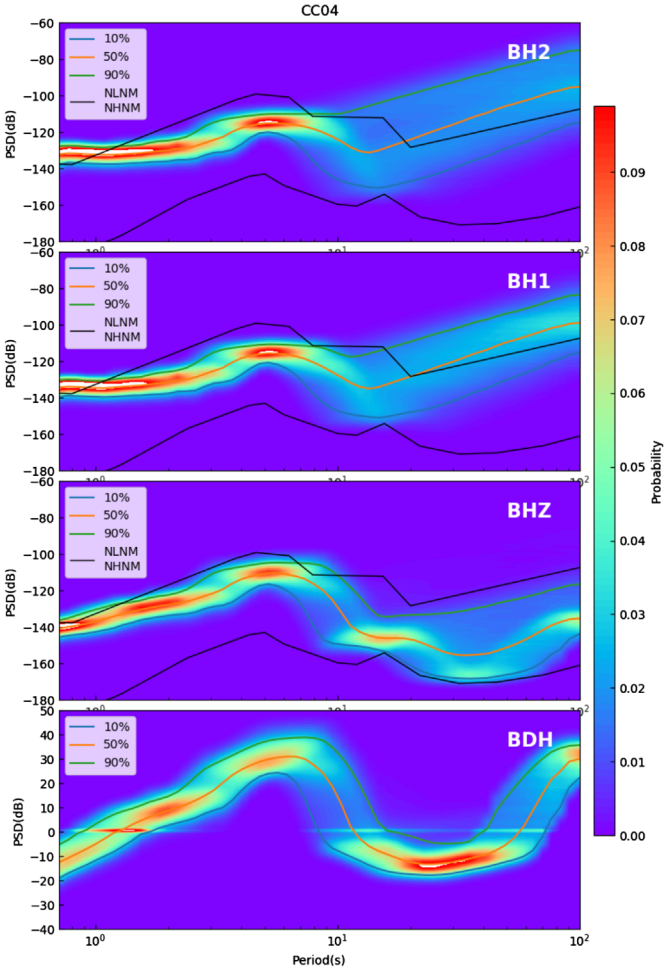

Figure 5. Probability density functions for hourly velocity power spectra calculated at station CC04 on all channels. The 10%, 50%, and 90% probability percentiles of the power are shown, as are the Peterson new low noise model (NLNM) and new high noise model (NHNM) for benchmark comparison (Peterson, 1993). Units for the seismic channels are relative to 1 (m/s)/Hz, and units for the pressure channel are relative to 1 Pa/Hz. The color version of this figure is available only in the electronic edition.

stations in the dataset (Fig. 5, supplemental materials F3, F4). These show several features expected for BBOBS stations. The spectral peak centered at ~6 s, visible on all four channels, is the secondary microseism, caused by nonlinear wave–wave interactions (Longuet-Higgins, 1950; Ardhuin *et al.*, 2011). The small peak centered at ~14 s, most visible on the BHZ and BDH channels, is the primary microseism. The primary microseism is muted relative to its appearance on land stations, because this signal is primarily generated at the coastlines. The log–linear increase in amplitude at periods ≥15 s on both BH1 and BH2 components is due to current-induced noise, which predominates the horizontal channels of correctly leveled seismometers. Finally, the strong peak at periods >60 s on the BDH (and, to lesser extent, the BHZ) channels marks the effect of seafloor compliance under the influence of infragravity wave forcing (e.g., Crawford *et al.*, 1991). Most stations manifest good coherence between the BHZ and BDH channels in the compliance band (~60–150 s, for the 4000–5500 m depths in these experiments). Thus, it is possible to use the pressure channel to remove compliance noise from the vertical channel within that band (e.g., Webb and Crawford, 2010). We show a proof-of-concept for this process in Figure 6, in which we also apply a correction using the horizontal channels that removes the effect of current noise on the vertical component due to instrument tilt. This analysis was done using the ATaCR code (Janiszewski *et al.*, 2019), which we recommend to users of 3+1

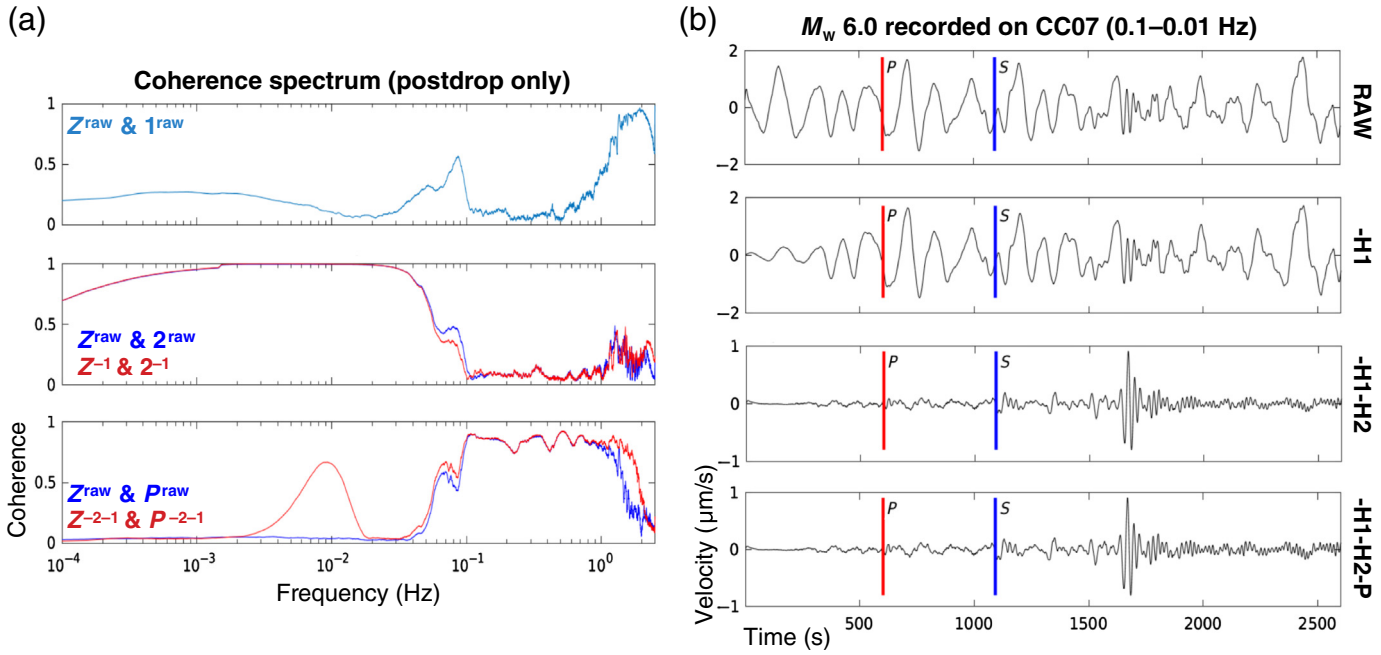

Figure 6. Demonstration of coherency between seismic and pressure channels, and use of noise stationarity to remove tilt and compliance effects from the vertical component. (a) Coherence between different channels of station CC07, before and after cleaning. Terminology "X^a and Y^b" indicates the coherence between channels X and Y, in which the former has been corrected using channel(s) "a" and the latter using channel(s) "b". (b) The vertical trace sequentially and cumulatively corrected for noise on horizontal channel 1, horizontal channel 2, and the pressure channel. The H2 correction is the most significant for noise removal, indicating maximal tilt in this direction. The predicted arrival times of *P* and *S* waves from an M_w 6.0 earthquake ~60° from the array are shown; prior to noise correction, it is impossible to make out body waves, and the surface waves are unrecognizable. After noise correction, the earthquake signals are clear. The color version of this figure is available only in the electronic edition.

component BBOBS+DPG data. For several of these stations, tilt noise is especially problematic; Figure 6 shows that, before horizontals' corrections are applied, there is very little vertical-pressure coherence, but the vertical is highly coherent with the horizontal channels. After the tilt effects are removed, the effects of infragravity compliance stand out.

Many of these stations are remarkably quiet, with low-noise floors for vertical and horizontal components. We record both teleseismic earthquakes and ambient noise, the latter through cross correlating and stacking data between pairs of stations (Fig. S1). An example of an M_w 6.8 teleseismic earthquake recorded across the Old ORCA array is shown in Figure 7, in which the normalized vertical records are aligned by distance from the event. Figure 8 shows data from an M_w 7.1 teleseismic *P*-wave arrival recorded on the Young ORCA array, illustrating the capability of this dataset for measuring differential travel times. This arrival was observed clearly on both vertical and pressure components, suggesting that the latter can be used to complement, or stand in for, the former during time periods when seismic data were absent or unreliable due to sensor problems. Intriguingly, a strong *T* phase is seen on the vertical and pressure channels of Old ORCA following large earthquakes (e.g., Fig. S5), demonstrating the low-noise floor of the pressure sensor. The seismic data will be used for a variety of seismic imaging methods to probe the oceanic mantle structure, including receiver functions, body-wave tomography, surface-wave anisotropic upper-mantle imaging. Moreover, these data provide new unique ray paths to help constrain global seismological models, which have a particular paucity of coverage in the southern hemisphere.

The new multibeam bathymetry mapping provides constraints on the nature of the oceanic crust and lithosphere, especially for the Young ORCA region where such data were previously nonexistent. The seafloor beneath Young ORCA has an average depth of 4620 m, with height variations dominated by abyssal hill topography with root mean square (rms) variability of order 100 m. The abyssal-hill structure is complemented by distinct seamounts and apparent volcanic ridges that reach depths as shallow as 3570 m. In detail, the orientation of the abyssal-hill fabric shows abrupt regional changes within the footprint. In the northern and southern regions, the fabric is oriented roughly 15° west of north, consistent with the seafloor-spreading direction inferred from the bounding fracture zones. Within an ~100 km band trending southeast between 5° and 7° S, the abyssal-hill fabric is oriented ~15° east of north, rotated roughly 30° from the surrounding regions and 60° from the inferred spreading direction. Where they are mapped, the along-strike transitions between the two fabric

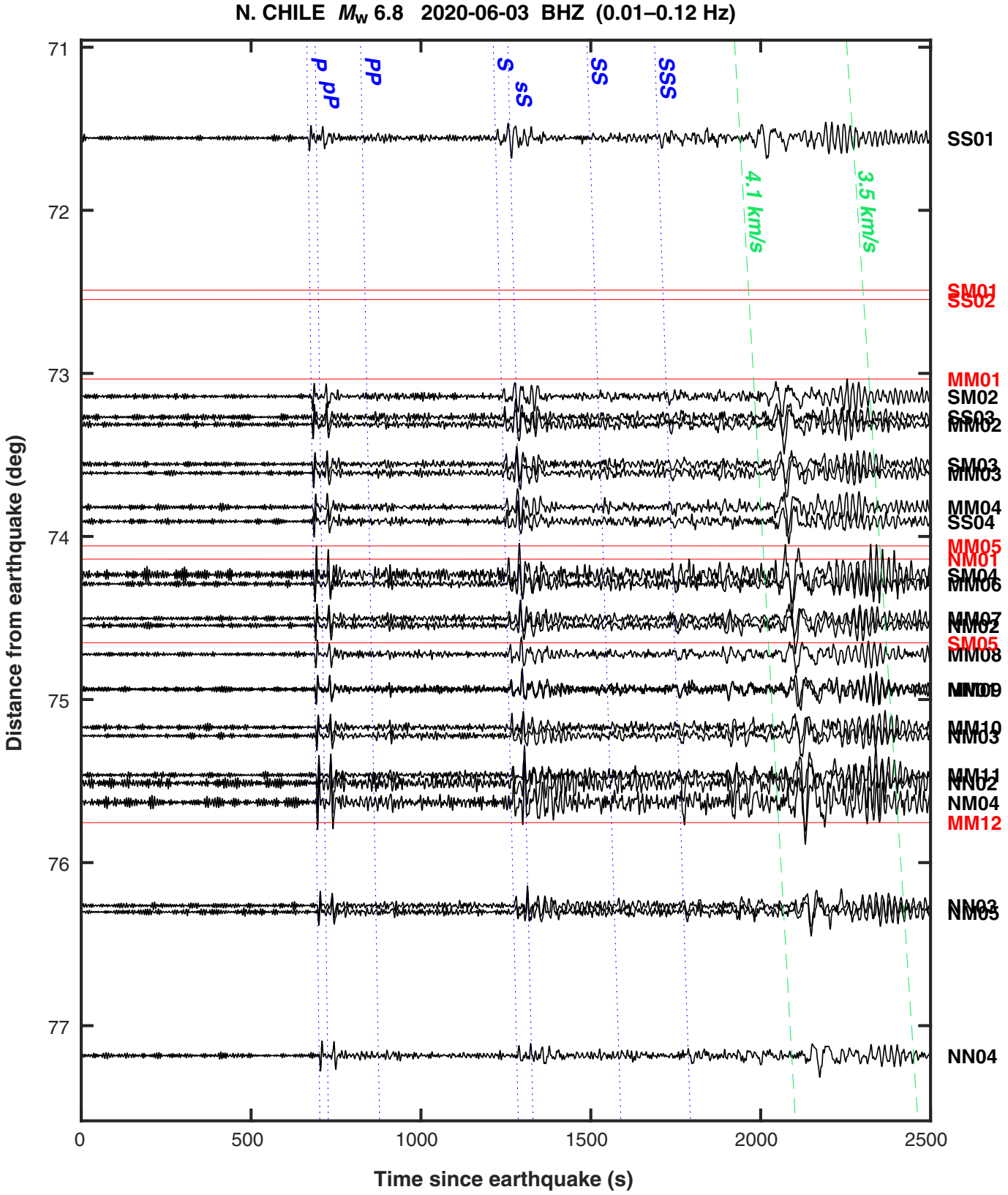

Figure 7. Record section of an M_w 6.8 earthquake in Chile (23.28° S, 68.47° W, 112 km depth) captured on the Old ORCA array; vertical-component shown, filtered from 0.01 to 0.12 Hz. Blue lines show arrival times and moveout for a variety of body-wave phases, and the 3.5–4.1 km/s (surface wave) phase velocity window is highlighted. Stations with null or bad data are shown in red. The color version of this figure is available only in the electronic edition.

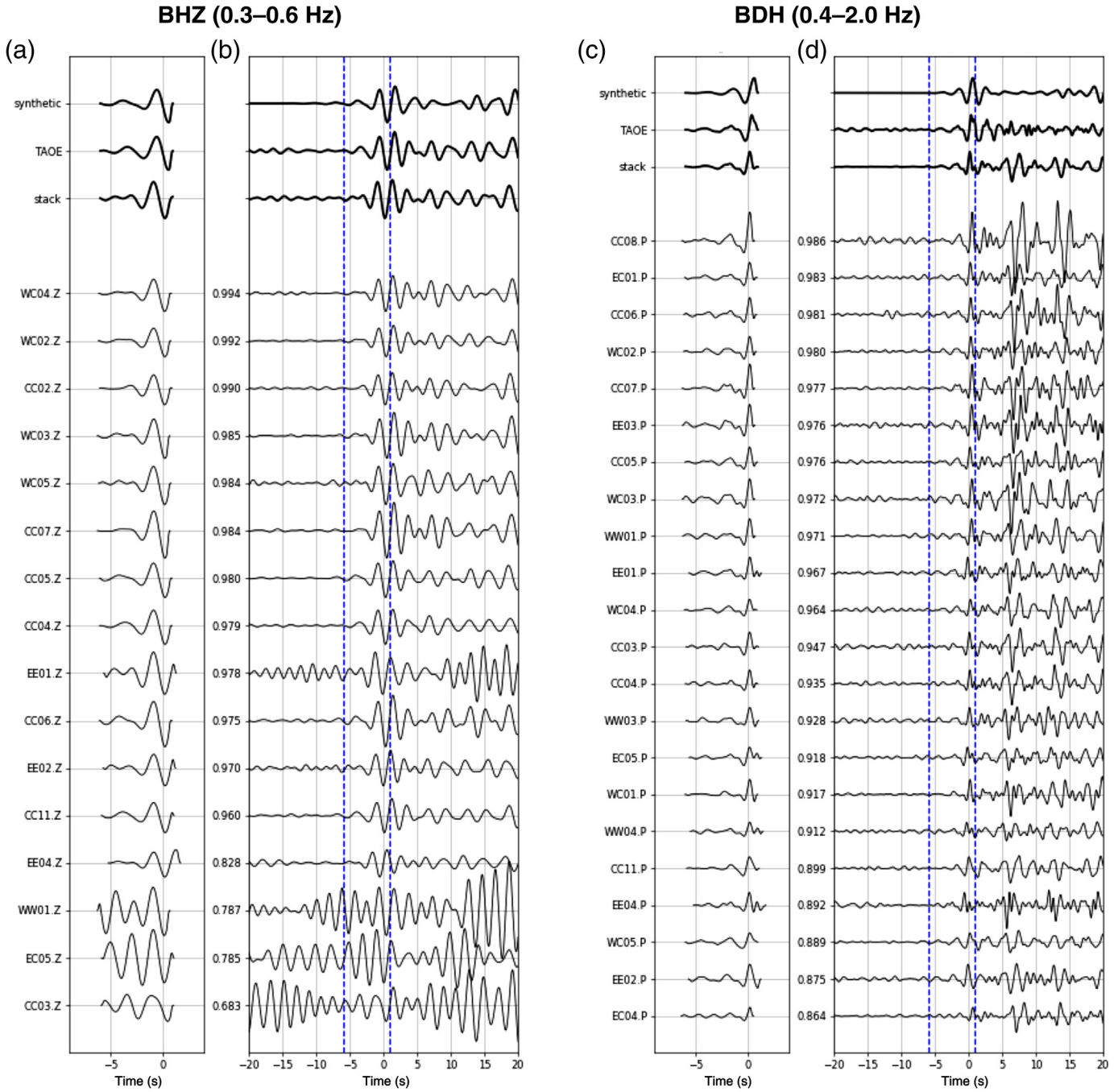

Figure 8. Example of *P*-wave differential travel-time computation using multichannel cross correlation (VanDecar and Crosson, 1990), for an M_w 7.1 earthquake (61.35° N, 149.96° W, 46.7 km depth) on 30 November 2018 recorded across the Young ORCA array (approximately 70° away). (a,b) Vertical-component (BHZ) seismometer data aligned by maximum cross correlation and filtered from 0.3 to 0.6 Hz with a four-pole Butterworth filter, chosen to avoid high-frequency noise evident on some seismic channels. Blue lines in (b) show hand-picked window used for cross correlations, with zoomed-in view of this data shown in (a). The three bold traces at the top correspond (from top down) to the synthetic data from syngine (computed using axisymmetric Spectral Element Method; Nissen-Meyer *et al.*, 2014), data from ~860 km distant station TAOE, located on Nuku Hiva in the Marquesas Islands, and the stack of the aligned data subsequently. The similarity between these waveforms is taken as evidence that this data are high quality and conforms to regional predictions; (c,d) for (a,b) but show DPG seismic data (BDH), and have a slightly different filter: 0.3–2 Hz due to different noise characteristics (compare with Fig. 3, supplemental files F1, F2). For the BDH comparison, the syngine and TAOE data are the negative of the vertical traces, which are expected to be 180° out of phase with pressure channel signals. Station names are provided at left, and the small numbers between the two pairs of columns indicate the maximum cross-correlation coefficient between each individual waveform and the array stack. The color version of this figure is available only in the electronic edition.

orientations are relatively smooth, and the anomalous fabric persists across the entire ~5 Ma spreading history spanned by the experiment. We infer a period of persistent oblique spreading during the formation of the crust in this region. In the north central portion of the array footprint, we mapped a system of en echelon valleys and associated sharp ridges, which reach a maximum depth of 5690 m and extend linearly for up to ~80 km. The valleys and ridges strike approximately 30° west of north, oblique to both orientations of abyssal-hill fabric as well as the bounding fracture zone to the north. We infer that these features likely postdate crustal formation at the ridge, and perhaps result from stresses associated with a reorganization of the adjacent ridge segment around 20 Ma (Müller *et al.*, 2008), roughly 20 My after crust formation. Finally, on a regional scale, the southwestern portion of the array is slightly elevated compared to half-space cooling predictions, presumably due to the influence of the Marqueses hotspot.

The new multibeam bathymetry from the Old ORCA array has an average depth of 5280 m, with height variations dominated by a combination of abyssal hill topography and volcanic ridges and seamounts that reach depths as shallow as 2500 m, with overall rms variability of order 240 m. Seamounts and other volcanic features are the most prominent in the northern half of the footprint, where the mean depth is slightly shallower (5200 m). The southern half of the array is deeper (mean of 5400 m), with fewer obvious volcanic edifices and lower rms topographic variability (170 m). The dominant orientation of the abyssal-hill fabric has an azimuth of ~70°, implying a fossil spreading direction of 160°, but there are small-scale variations spanning azimuths of ~45°–90° that suggest second-order segmentation processes during seafloor spreading. Basalts dredged from several of the seamounts are being dated and analyzed for geochemical provenance by Matthew Jackson at UC Santa Barbara. Rock samples are archived at the UC San Diego SIO Geological Collections Database.

Initial Results

We have determined the horizontal channel azimuths (sensor orientation) of all seismometers in the dataset for which normal horizontal data are available. This analysis was performed using the Rayleigh-wave method (Stachnik *et al.*, 2012; Doran and Laske, 2017), grid searching through all possible azimuths to find the orientation that best correlated the vertical and Hilbert-transformed radial channels at zero lag (Fig. S3). On average, 20 $M_w > 6.0$ teleseismic earthquakes were used for this analysis, and the final orientation was determined from a weighted average of event-wise estimates, weighting by the maximum cross-correlation coefficient. The orientations are given in Table 1 with additional details in Supplemental Table S1.

Initial analyses confirm that these data provide useful constraints on upper mantle anisotropic velocity structure. The aperture of the arrays, even considering station drop outs, is sufficient to measure Rayleigh-wave phase velocities from 3 to 150 s, using both earthquakes and ambient noise (Fig. S1; Russell, 2020; Phillips *et al.*, 2021; Russell *et al.*, 2021). Ambient-noise Love waves are clearly observed from 4 to 9 s (Russell, 2020; Phillips *et al.*, 2021; Russell *et al.*, 2021), despite the generally noisy horizontal channels, in particular at Young ORCA. These data will also allow body-wave tomography with sensitivity from ~70 to 400 km (Fig. 8; Eilon *et al.*, 2021a). Preliminary *P*-wave receiver function analysis shows clear signals from the oceanic Moho and the water column multiples (Eilon *et al.*, 2021b). Unfortunately, the noisy horizontal components on the Young ORCA array preclude *S*-wave receiver functions, and this analysis constitutes future work for the Old ORCA array.

Summary

The ORCA dataset represents a substantial expansion of high-quality passive seismic data in the central and southern Pacific Ocean basin. Two 30-instrument arrays yielded ~13 months of data each from broadband seismic sensors and DPGs. The overall data recovery rate from the Young ORCA array (on ~40 Ma crust) was 68%, but several stations suffered from a variety of engineering problems that cut short data logging and in some cases compromised data quality. The data recovery rate from the Old ORCA array (on ~120 Ma crust) was 80%, and the 97% DPG data recovery affords a continuous seismic dataset at all 30 stations for >10 months. The quality of the data, particularly that of Old ORCA, is high, and a variety of passive source seismological studies will be feasible with this data. These arrays expand seismic coverage far into previously uninstrumented tracts of the Pacific basin, providing new ray geometries for global seismology, as well as detailed examination of Earth structure within the deployment footprints. The complementary multibeam bathymetry and underway geophysical datasets offer significant potential for detailed multifaceted examinations of these two regions.

Data and Resources

The seismic data from this experiment are available through the Incorporated Research Institutions for Seismology's Data Management Center (IRIS-DMC) under the network codes XE (2018–2019) and 7B (2019–2020). Multibeam swath bathymetry data and other underway data collected are available via the Rolling Deck to Repository (R2R) portal (in chronological order, dois are 10.7284/907958, 10.7284/908257, 10.7284/908280, 10.7284/908890). The supplemental material to this article contains Figures S1–S5, which provide (S1–2) illustration of clock drift calculations, (S3) an example of ocean-bottom seismometer (OBS) orientation estimates using Rayleigh-wave polarization, (S4) the data status for all stations, and (S5) a *T*-phase record section. It also includes supplemental Table 1, with orientation estimates of all instruments. Finally, the supplemental material includes descriptions of F1–F7, which provide users with comprehensive information about data status, quality, and response for all stations in the dataset. Processed multibeam surfaces are stored as netCDF grids for the Young ORCA location (doi: 10.26022/IEDA/329885)

Declaration of Competing Interests

The authors acknowledge that there are no conflicts of interest recorded.

Acknowledgments

This work was funded by National Science Foundation (NSF) grants OCE-1658491, OCE-1658214, OCE-1658070, and OCE-2051265. The broadband ocean-bottom-seismometer (BBOBS) instruments were provided by the Scripps Institution of Oceanography (SIO) ocean-bottom-seismometer (OBS) facility under Jeffrey Babcock, with oversight and logistical support from John Collins and Masako Tominaga at the OBS Instrument Center. The authors are deeply grateful to techs that sailed on these cruises: Mark Gibaud, Ernest Aaron, Sean McPeak, Justin Smith, and Pete Liljegren. The authors are indebted to the captains and crews of the R/V Kilo Moana and R/V Roger Revelle, ResTechs and OTGs (Julianna Diehl, Jeff Kochs, Trevor Young, Rob Palomares, Mary Huey, Andrew Naslund, Josh Manger, and Royhon Agostine), and well as the ship scheduling and logistical assistance from Bruce Applegate and Hannah Delapp, who enabled us to conduct safe science during a pandemic. Finally, the authors thank the other members of the science parties: Helen Janiszewski, William Hawley, Brennan Brunsvik, Lindsay Buff, Caroline Eakin, Gareth Fabbro, Isabella Gama, Karen Godfrey, Eva Golos, Carlos Gomez, Rachel Hatch, Emily Hopper, Yuki Kawano, Aditya Khare, Taylor Lee, Jumpei Maruyama, Marshal McGurk, Stephen Mosher, Erica Nathan, Engielle Mae Paguican, Mohan Pan, Ashley Rivera, Kaelynn Rose, Theresa Sawi, Eivind Straume, Veselina Yakimova, and Kim Chu-Fang Yang.

References

Ardhuin, F., E. Stutzmann, M. Schimmel, and A. Mangeney (2011). Ocean wave sources of seismic noise, *J. Geophys. Res.* **116,** no. C9, C09004, doi: 10.1029/2011jc006952.

Ballmer, M. D., J. van Hunen, G. Ito, T. A. Bianco, and P. J. Tackley (2009). Intraplate volcanism with complex age-distance patterns: A case for small-scale sublithospheric convection, *Geochem. Geophys. Geosys.* **10,** no. 6, doi: 10.1029/2009GC002386/epdf.

Buck, W. R., and E. M. Parmentier (1986). Convection beneath young oceanic lithosphere: Implications for thermal structure and gravity, *J. Geophys. Res.* **91,** no. B2, 1961–1974, doi: 10.1029/jb091ib02p01961.

Cox, C., T. Deaton, and S. C. Webb (1984). A deep-sea differential pressure gauge, *J. Atmos. Ocean. Tech.* **1,** 237–246.

Crawford, W. C., S. C. Webb, and J. A. Hildebrand (1991). Seafloor compliance observed by long-period pressure and displacement measurements, *J. Geophys. Res.* **96,** no. B10, 16,151–16,160.

Doran, A. K., and G. Laske (2017). Ocean-bottom seismometer instrument orientations via automated Rayleigh-wave arrival angle measurements, *Bull. Seismol. Soc. Am.* **107,** no. 2, 691–708, doi: 10.1785/0120160165.

Eilon, Z. C., L. Zhang, J. B. Russell, J. B. Gaherty, and D. W. Forsyth (2021a). Small scale mantle convection imaged by the ORCA array, *PacificArray Workshop 2021*, University of Tokyo, Tokyo, 28 May 2021.

Eilon, Z. C., L. Zhang, J. B. Russell, J. B. Gaherty, and D. W. Forsyth (2021b). New results from the Pacific ORCA (OBS Research into Convecting Asthenosphere) experiment, *Marine Seismology Symposium, Mantle Dynamics and Imaging Posters*, 11 March 2021.

Gouédard, P., T. Seher, J. J. McGuire, J. A. Collins, and R. D. van der Hilst (2014). Correction of ocean-bottom seismometer instrumental clock errors using ambient seismic noise, *Bull. Seismol. Soc. Am.* **104,** no. 3, 1276–1288.

Hable, S., K. Sigloch, G. Barruol, S. C. Stähler, and C. Hadziioannou (2018). Clock errors in land and ocean bottom seismograms: High-accuracy estimates from multiple-component noise cross-correlations, *Geophys. J. Int.* **214,** 2014–2034, doi: 10.1093/ GJI/GGY236.

Hannemann, K., F. Krüger, and T. Dahm (2014). Measuring of clock drift rates and static time offsets of ocean bottom stations by means of ambient noise, *Geophys. J. Int.* **196,** no. 2, 1034–1042.

Haxby, W. F., and J. K. Weissel (1986). Evidence for small-scale mantle convection from Seasat altimeter data, *J. Geophys. Res.* **91,** 3507–3520, doi: 10.1029/jb091ib03p03507.

Janiszewski, H. A., J. B. Gaherty, G. A. Abers, H. Gao, and Z. C. Eilon (2019). Amphibious surface-wave phase-velocity measurements of the Cascadia subduction zone, *Geophys. J. Int.* **217,** no. 3, 1929–1948, doi: 10.1093/gji/ggz051.

Janiszewski, H. A., J. B. Russell, W. B. Hawley, Y. J. Tan, C. Lynner, J. B. Gaherty, Z. Eilon, and S. Mosher (2020). 10+ years of ocean bottom seismic noise: New insights and remaining questions, *AGU Fall Meeting 2020*, 1–17 December 2020, #S059-01.

Kawakatsu, H., J. B. Gaherty, H. Utada, S.-M. Lee, Y. K. Kim, and Z. Eilon (2019). New progress in building Pacific Array: An international collaboration to image mantle dynamic processes across the Pacific basin, *AGU Fall Meeting 2019*, #DI11A-01.

Longuet-Higgins, M. S. (1950). A theory of the origin of microseisms, *Phil. Trans. Roy. Soc. Lond. Math. Phys. Sci.* **243,** no. 857, 1–35.

Müller, R. D, M. Sdrolias, C. Gaina, and W. R. Roest (2008). Age, spreading rates, andspreading asymmetry of the world's ocean crust, *Geochem. Geophys. Geosys.* **9,** no. 4, doi: 10.1029/2007GC001743.

National Oceanic and Atmospheric Administration [NOAA] National Geophysical Data Center (2009). *ETOPO1 1 Arc-Minute Global Relief Model*, NOAA National Centers for Environmental Information, Accessed 08-02-16.

Nissen-Meyer, T., M. van Driel, S. C. Stähler, K. Hosseini, S. Hempel, L. Auer, A. Colombi, and A. Fournier (2014). AxiSEM: Broadband 3-D seismic wavefields in axisymmetric media, *Solid Earth* **5,** 425–445, doi: 10.5194/se-5-425-2014.

Peterson, J. R. (1993). Observation and modeling of seismic background noise, *U.S. Geol. Surv. Open-File Rept. No. OF 93-0322*, doi: 10.3133/ofr93322.

Phillips, J., J. B. Gaherty, Z. C. Eilon, J. B. Russell, and D. W. Forsyth (2021). Ambient noise tomography of 120 Ma oceanic lithosphere in the southwest Pacific, *PacificArray Workshop 2021*, University of Tokyo, Tokyo, 28 May 2021.

Russell, J. B. (2020). Structure and evolution of the oceanic lithosphere-asthenosphere system from high-resolution surface-wave imaging, *Ph.D. Thesis*, Columbia University, New York, New York, 201 pp.

Russell, J. B., Z. C. Eilon, and S. G. Mosher (2019). OBSrange: A new tool for the precise remote location of ocean-bottom seismometers, *Seismol. Res. Lett.* **90,** no. 4, 1627–1641, doi: 10.1785/0220180336.

Russell, J. B., J. B. Gaherty, Z. C. Eilon, D. W. Forsyth, and G. Ekström (2021). Age dependence of mantle shear velocity and anisotropy in the central Pacific: Implications for thermal evolution of the lithosphere and small-scale convection, *Marine Seismology Symposium 2021: Mantle Dynamics and Imaging Posters*, 11 March 2021.

Ryan, W. B. F., S. M. Carbotte, J. O. Coplan, S. O'Hara, A. Melkonian, R. Arko, R. A. Weissel, V. Ferrini, A. Goodwillie, F. Nitsche, *et al.* (2009). Global multi-resolution topography synthesis, *Geochem. Geophys. Geosys.* **10,** Q03014, doi: 10.1029/2008GC002332.

Sandwell, D., and Y. Fialko (2004). Warping and cracking of the Pacific plate by thermal contraction, *J. Geophys. Res.* **109,** no. B10, doi: 10.1029/2004jb003091.

Sandwell, D. T., R. D. Müller, W. H. F. Smith, E. Garcia, and R. Francis (2014). New global marine gravity model from CryoSat-2 and Jason-1 reveals buried tectonic structure, *Geochem. Geophys. Geosys.* **346,** no. 6205, 65–67, doi: 10.1126/science.1258213.

Seton, M., R. D. Müller, S. Zahirovic, S. Williams, N. M. Wright, J. Cannon, J. M. Whittaker, K. J. Matthews, and R. McGirr (2020). A global data set of present-day oceanic crustal age and seafloor spreading parameters, *Geochem. Geophys. Geosys.* **21,** no. 10, e2020GC009214, doi: 10.1029/2020GC009214.

Stachnik, J. C., A. F. Sheehan, D. W. Zietlow, Z. Yang, J. Collins, and A. Ferris (2012). Determination of New Zealand ocean bottom seismometer orientation via rayleigh-wave polarization, *Seismol. Res. Lett.* **83,** no. 4, 704–713, doi: 10.1785/0220110128.

Stehly, L., M. Campillo, and N. M. Shapiro (2007). Traveltime measurements from noise correlation: Stability and detection of instrumental time-shifts, *Geophys. J. Int.* **171,** no. 1, 223–230.

VanDecar, J. C., and R. S. Crosson (1990). Determination of teleseismic relative phase arrival times using multi-channel cross-correlation and least squares, *Bull. Seismol. Soc. Am.* **80,** no. 1, 150–169.

Webb, S. C. (1998). Broadband seismology and noise under the ocean, *Rev. Geophys.* **36,** 105–142.

Webb, S. C., and W. C Crawford (2010). Shallow-water broadband OBS seismology, *Bull. Seismol. Soc. Am.* **100,** no. 4, 1770–1778, doi: 10.1785/0120090203.

Weeraratne, D. S., E. M. Parmentier, and D. W. Forsyth (2003). Viscous fingering of miscible fluids in laboratory experiments and the oceanic mantle asthenosphere, *EOS Transactions, American Geophysical Union, Fall Meeting Supplement*, Abstract Id: V21B-03, 84 pp.

Manuscript received 30 June 2021
Published online 20 October 2021